The Astrophysical Journal, 750:74 (11pp), 2012 May 1 doi:10.1088/0004-637X/750/1/74

NEW H_2 COLLISION-INDUCED ABSORPTION AND NH_3 OPACITY AND THE SPECTRA OF THE COOLEST BROWN DWARFS

Didier Saumon[1], Mark S. Marley[2], Martin Abel[3], Lothar Frommhold[3], and Richard S. Freedman[4,5]
[1] Los Alamos National Laboratory, P.O. Box 1663, Mail Stop F663, Los Alamos, NM 87545, USA; dsaumon@lanl.gov
[2] NASA Ames Research Center, Mail Stop 245-3, Moffett Field, CA 94035, USA; Mark.S.Marley@nasa.gov
[3] Physics Department, University of Texas at Austin, Austin, TX 78712, USA; mabel@physics.utexas.edu, frommhold@physics.utexas.edu
[4] SETI Institute, 515 Whisman Road, Mountain View, CA 94043, USA; freedman@darkstar.arc.nasa.gov
[5] Space Science and Astrobiology Division, NASA Ames Research Center, Mail Stop 245-3, Moffett Field, CA 94035, USA
Received 2011 December 21; accepted 2012 February 27; published 2012 April 17

ABSTRACT

We present new cloudy and cloudless model atmospheres for brown dwarfs using recent ab initio calculations of the line list of ammonia (NH_3) and of the collision-induced absorption of molecular hydrogen (H_2). We compare the new synthetic spectra with models based on an earlier description of the H_2 and NH_3 opacities. We find a significant improvement in fitting the nearly complete spectral energy distribution of the T7p dwarf Gliese 570D and in near-infrared color–magnitude diagrams of field brown dwarfs. We apply these new models to the identification of NH_3 absorption in the *H*-band peak of very late T dwarfs and the new Y dwarfs and discuss the observed trend in the NH_3–*H* spectral index. The new NH_3 line list also allows a detailed study of the medium-resolution spectrum of the T9/T10 dwarf UGPS J072227.51−054031.2 where we identify several specific features caused by NH_3.

Key words: brown dwarfs – opacity – stars: atmospheres

Online-only material: color figures

1. INTRODUCTION

Brown dwarfs, with masses between ∼0.01 and 0.075 $M_\odot$, are not massive enough to maintain steady hydrogen fusion in their cores and, except when they are very young, have effective temperatures below that of main-sequence stars. Their low atmospheric temperatures allow the formation of molecules and condensates that leave conspicuous imprints on their spectral energy distribution (SED) that have led to the creation of two spectral classes: the L dwarfs with $T_{\rm eff} \sim$ 2400–1400 K (Kirkpatrick 2005) and the cooler T dwarfs extending down to $T_{\rm eff} \sim$ 500 K (Leggett et al. 2010a). The recent discovery of several extremely cool dwarfs by the *Wide-field Infrared Survey Explorer* (*WISE*) motivates the creation of a new spectral class: the Y dwarfs with $T_{\rm eff} \lesssim$ 500 K (Cushing et al. 2011).

The spectra of L dwarfs are characterized by absorption bands of VO, TiO, H_2O, CO, FeH, CrH, and the very broad doublets of Na I (0.59 μm) and K I (0.77 μm) (Kirkpatrick et al. 1999). While condensates, primarily corundum, magnesium silicates, and iron, do not have spectral features as distinctive as those of molecules, their continuum opacity reddens the near-infrared spectrum of L dwarfs significantly. The effects of the cloud opacity on the SEDs of brown dwarfs peak at $T_{\rm eff} \sim$ 1500–1600 K (spectral types L6–L8). In the cooler T dwarfs, the condensate cloud layer sinks below the photosphere, TiO and VO have been lost to TiO_2, for VO_2 and condensates (Burrows & Sharp 1999; Lodders 2002) the carbon chemistry has shifted to favor CH_4 (Burgasser et al. 2002; Lodders & Fegley 2002), and NH_3 bands appear in the mid-infrared around T2 (Cushing et al. 2006). In the very latest T dwarfs and in the new Y dwarfs, weak bands of NH_3 appear in the near-infrared (Delorme et al. 2008; Cushing et al. 2011).

Due to their additional degrees of freedom and greater complexity, the opacities of molecules are not nearly as well understood as those of atoms and ions. The primary molecular opacity data bases are the HITRAN (Rothman et al. 2003, 2005, 2009) and the GEISA (Jacquinet-Husson et al. 1999, 2005) compilations, which were developed for modeling Earth's atmosphere and consider the opacity of gases at temperatures of 300 K and below. Since the temperature in brown dwarf atmospheres can be up to 10 times higher, those line lists are missing the so-called hot bands that arise from the absorption of a photon from an excited lower level that is not thermally populated at 300 K. In some cases, the molecular line spectrum is so rich that individual transitions are unresolved in laboratory spectra or it becomes impossible to assign the observed transitions to specific molecular energy levels. The line lists are thus incomplete for the conditions encountered in brown dwarf atmospheres, especially for higher photon energies, hot bands, and weak transitions corresponding to near-infrared and optical wavelengths. Incomplete molecular line lists limit the predictive capability of atmosphere models and synthetic spectra of brown dwarfs (Cushing et al. 2008; Stephens et al. 2009), a problem that was recognized in the first attempts to model the observed spectrum of a brown dwarf, the T7p dwarf Gliese 229B (Marley et al. 1996; Allard et al. 1996). In view of the difficulties in analyzing laboratory spectra of high temperature molecular gases, an alternative is to compute a molecular line list with a first-principles approach.

The past 15 years of brown dwarf research have motivated the theoretical modeling of the opacity of several key molecules. New molecular line lists for H_2O (Partridge & Schwenke 1997; Barber et al. 2006), CO (Goorvitch 1994), TiO (Schwenke 1998), VO (Plez 1998), FeH (Dulick et al. 2003), CrH (Burrows et al. 2002), have improved the quality of the brown dwarf model spectra significantly. Methane (CH_4) has been and remains the most important molecule observed in brown dwarf spectra (defining the T spectral class, but appearing as early as L5; Noll et al. 2000) with a very incomplete line list at near-infrared wavelengths, although some progress has been made (Freedman et al. 2008; Schwenke 2002). The two most recent developments in this area are new calculations of a line list of ammonia (NH_3) and of the continuum opacity from collision-induced absorption (CIA) by H_2 molecules.

We study the effect of both of these much anticipated opacity calculations on the spectra and colors of brown dwarfs. In

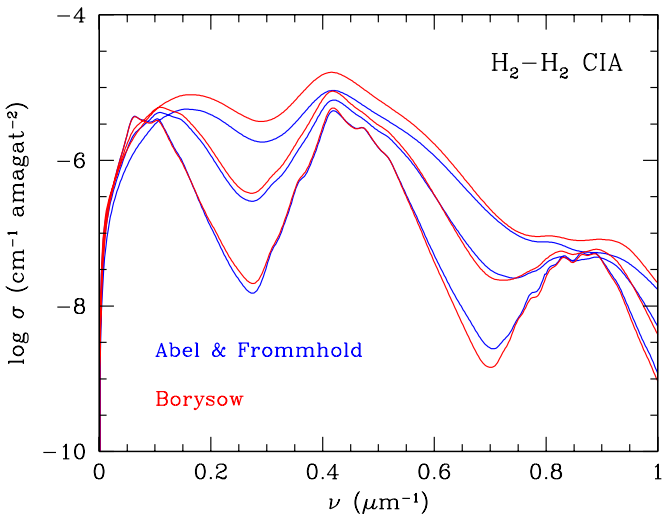

Figure 1. Collision-induced absorption coefficient for H_2–H_2 collisions at $T = 500$, 1000, and 2000 K, from bottom to top, respectively. Each broad peak corresponds to a change in the vibrational quantum number of $\Delta\upsilon = 0, 1, 2,...$ from left to right, respectively. The calculations of Borysow and collaborators (Borysow et al. 2001; Borysow 2002, and references therein) and the recent work of Abel and Frommhold (Frommhold et al. 2010; Abel et al. 2011) are shown in red and blue, respectively. 1 amagat $= 2.6867774 \times 10^{19}$ cm^{-3}.

(A color version of this figure is available in the online journal.)

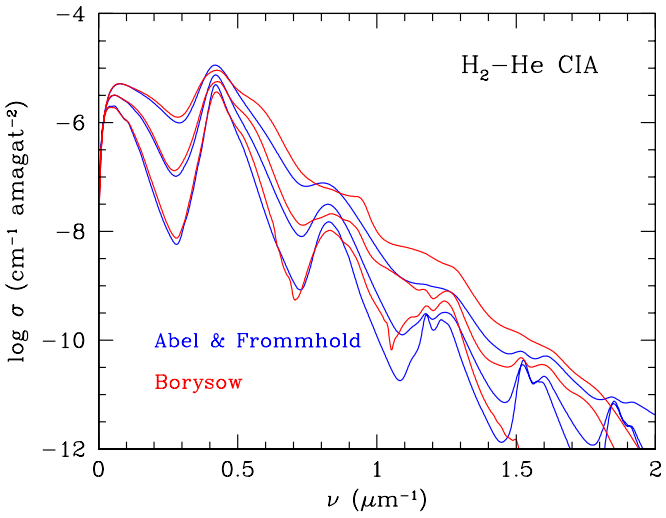

Figure 2. Same as Figure 1 for H_2–He CIA. The older calculation labeled "Borysow" is from Borysow et al. (1989), Jorgensen et al. (2000), and references therein. The "Abel & Frommhold" calculation is from Abel et al. (2012).

(A color version of this figure is available in the online journal.)

Section 2, we discuss the nature of H_2 CIA opacity, how the new calculation changes the opacity, and how it affects the SED of cool brown dwarfs. The role of the NH_3 opacity in brown dwarf spectra is presented in Section 3, where we show how the new line list for NH_3 affects primarily the near-infrared spectrum and brings new spectral features that can help define the T/Y dwarf boundary. We demonstrate the resulting improvement in synthetic spectra by comparing with the well-characterized SED of the T7.5 dwarf Gliese 570D and near-infrared color–magnitude diagrams in Section 4. The improved NH_3 line list provides the opportunity to comment on the role of ammonia in extremely cool dwarfs near the T/Y transition and on recent detections of this molecule in the spectra of extreme objects (Section 5). Concluding remarks are provided in Section 6.

2. COLLISION-INDUCED ABSORPTION BY H_2

Molecular hydrogen H_2 is the most abundant component of brown dwarf atmospheres. Because of its high degree of symmetry, the H_2 molecule has no permanent dipole moment and only quadrupole transitions are allowed, which are very weak. During a collision with another particle, however, the compound H_2-particle system has a temporary dipole moment and can thus undergo a radiative dipole transition. The CIA process is significant only at relatively high densities where collisions are frequent, such as in the atmospheres of planets and brown dwarfs. Three-body and higher-order collisions also contribute to CIA but are probably negligible in brown dwarf atmospheres (Hare & Welsh 1958).

While the probability of a dipole transition in a typical molecule involves only molecular properties, CIA also depends on the frequency of collisions with other atoms or molecules (primarily other H_2 and He, by far the most abundant species), which is linearly dependent on the density of the gas. For a given metallicity, the relative importance of CIA absorption in a brown dwarf atmosphere is a measure of the density of the gas, which is closely tied to the surface gravity. On the other hand, the importance of H_2 CIA decreases in higher metallicity atmospheres as the absorption from molecules involving heavier elements (CH_4, CO, H_2O, NH_3) becomes dominant. This sensitivity of H_2 CIA to gravity and metallicity is a useful spectral diagnostic in T dwarfs (Burgasser et al. 2002, 2003a; Burgasser 2004).

The H_2 CIA transitions occur between vibrational–rotational levels of the H_2 molecule and form a series of bands corresponding to $\Delta\upsilon = 0$, 1, 2, 3, etc., where υ is the vibrational quantum number of the molecule. Each band is formed by transitions between the different rotational levels for a given $\Delta\upsilon$. Collisional broadening of the individual lines is comparable to the line spacing, and thus H_2 CIA is effectively a continuum source of opacity. Borysow and her collaborators calculated the H_2–H_2 and H_2–He CIA coefficients in the temperature regime of interest for brown dwarf and white dwarf atmospheres (Borysow & Frommhold 1986a; Borysow et al. 1989, 2001; Jorgensen et al. 2000; Borysow 2002; Gustafsson & Frommhold 2003),[6] and those are universally used by brown dwarf modelers (Freedman et al. 2008; Sharp & Burrows 2007; Allard et al. 2001). The H_2–H_2 and H_2–He CIA coefficients are shown in Figures 1 and 2, respectively. While these two sources of opacity have similar frequency (ν) and temperature (T) dependences, H_2–He plays a secondary role since the collisions with He are about 10 times less frequent than with H_2 as follows from their relative number densities. The absorption coefficient per H_2 molecule is

$$\kappa_{H_2}(\nu, T) = n_{H_2}\sigma_{H_2-H_2}(\nu, T) + n_{He}\sigma_{H_2-He}(\nu, T), \qquad (1)$$

where n_i is the number density of species i and σ_{H_2-i} is the H_2-i CIA cross section. The successive CIA bands corresponding to $\Delta\upsilon = 0, 1, ...5$ are clearly visible in Figures 1 and 2. At higher temperatures, weaker transitions become more important and fill in the inter-band regions. The $\Delta\upsilon = 1$ band centered at $\sim$0.42 μm^{-1} (2.4 μm) is important in T dwarfs as it coincides with the K-band flux peak, which is caused by a minimum in the combined opacities of H_2O and CH_4. On the other hand, the J- and H-band flux peaks in the spectra of T dwarfs are shaped

[6] Additional H_2 CIA references as well as codes and tables can be found at http://www.astro.ku.dk/~aborysow/programs/index.html.

primarily by H_2O and CH_4 absorption. Thus, the K/J and K/H flux ratios reflect the relative importance of H_2 CIA to the H_2O and CH_4 opacities which are affected primarily by the gravity and metallicity of the atmosphere. A relatively weaker K-band flux indicates a higher gravity (stronger H_2 CIA) or a lower metallicity (weaker H_2O and CH_4 bands), or both. Our model atmospheres tend to underestimate the K-band flux, resulting in bluer $J-K$ than is observed for late T dwarfs (Saumon & Marley 2008). We have long suspected that this systematic offset comes form an overestimate of the strength of the H_2 CIA in the $\Delta\upsilon = 1$ band.

2.1. New Calculation of the H_2 Collision-induced Absorption

First-principles calculations of molecular opacities are typically conducted in two steps. First, a potential energy surface is calculated for a range of molecular geometries representing variations in bond lengths and bond angles. This potential surface, which is multi-dimensional for polyatomic molecules, is obtained by solving the quantum mechanical Schrödinger equation for the electrons for each given nuclear geometry using methods of quantum chemistry. The potential surface then serves as input for the calculation of the eigenstates of the molecule and the induced dipole moment surface from which allowed transitions and their oscillator strengths can be calculated to generate a line list. For bands originating from excited states, or for relatively high energy transitions (in the optical), the final state is well above the ground state of the molecule. The calculation of these lines requires an accurate knowledge of the potential energy surface far from the minimum that approximately corresponds to the ground state energy, which involves many subtle quantum mechanical effects and requires extensive calculations for widely separated configurations of nuclei. The calculation of higher energy transitions and of "hot bands" is thus increasingly difficult.

The growing evidence from brown dwarf spectra that something was amiss in the $\Delta\upsilon = 1$ band of H_2 CIA, as well as applications to ultracool white dwarfs (Bergeron et al. 1995), prompted a new calculation of the H_2–H_2 and H_2–He CIA opacity in the entire regime of temperatures and frequencies of interest (Frommhold et al. 2010; Abel et al. 2011, 2012). New, high accuracy potential energy surfaces and induced dipole surfaces were generated for these two CIA processes. The resulting opacity was calculated on a fine temperature and frequency grid, from $\nu = 20$ to 10^4 cm^{-1} and $T = 200$–3000 K for H_2–H_2 and 20 to 20,000 cm^{-1} and $T = 200$–9900 K for H_2–He (Richard et al. 2012). The H_2–H_2 table is being extended to the same (T, ν) grid as the H_2–He table. In each case, the entire parameter range is covered in a uniform manner, while earlier tabulations used different approximations and potential surfaces for different temperature and frequency ranges. As is the case for the older calculations, the new H_2–H_2 opacities are in excellent agreement with experimental data, which are limited to $T \leqslant 300$ K (Frommhold 1993; Abel et al. 2011). Comparisons with the CIA opacity previously used in modeling brown dwarf atmospheres are shown in Figures 1 and 2. As expected, differences are negligible or minimal at low temperatures. The differences become substantial at 2000 K in the roto-translational band for H_2–H_2 ($\sim$0.1–0.2 μm^{-1}) and in all roto-vibrational bands ($\Delta\upsilon > 0$). In the fundamental band ($\Delta\upsilon = 1$), which affects the K-band flux in brown dwarfs, the H_2–H_2 CIA has decreased by 24% at 1000 K and by 44% at 2000 K, which goes in the direction required to bring the K-band flux of the models into better agreement with the observations. The blue side of the fundamental band of H_2–H_2 CIA extends into the H photometric band where the absorption has decreased somewhat at temperatures above $\sim$1500 K. The H_2–He contribution (Figure 2) shows similar variations, except that the absorption coefficient increases at the peaks of the fundamental and first overtone bands. At frequencies above $\sim$1 μm^{-1}, the corrections can be factors of three or more. This matters less in brown dwarfs as H_2 CIA is not an important source of opacity at optical wavelengths and the He abundance is $\sim$10% that of H_2.

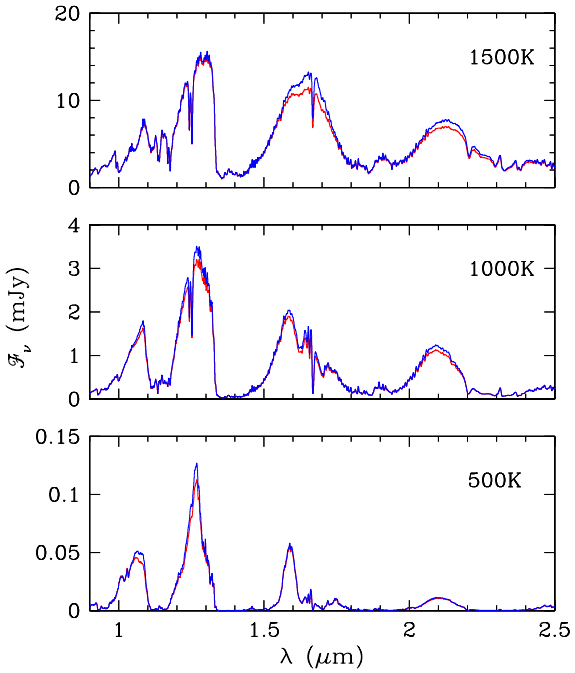

Figure 3. Effect of the new H_2–H_2 and H_2–He CIA opacity on synthetic spectra of brown dwarfs. The spectra shown are *cloudless* models with $T_{\rm eff} = 1500$, 1000, and 500 K, with $\log g = 5$ (cgs) and solar metallicity. The spectra computed with the new CIA opacities are shown in blue. The red lines show spectra computed with the older CIA opacity and the same (T, P) structures. The fluxes are calculated for $d = 10$ pc and are displayed at a resolving power of $R = 500$.

(A color version of this figure is available in the online journal.)

The effect of the change in the CIA opacity is shown in Figure 3 where spectra computed with the old and the new opacity, but with the same (T, P) atmospheric structures, are compared. All the flux peaks in the near-infrared are affected, with rather modest flux increases of $\lesssim$15%. Since the new H_2 CIA opacity is nearly identical to the older calculation at $T = 300$ K and increasingly differs at higher temperatures, the differences in the spectra tend to be larger at higher $T_{\rm eff}$ and nearly vanish for $T_{\rm eff} \lesssim 500$ K, except in the Y and J bands which are relatively transparent and probe the atmosphere at temperatures well above $T_{\rm eff}$. Since the CIA opacity increases with the gas density, i.e., with gravity, lower gravity spectra are less affected by the new CIA. For example, at $\log g = 4$ (cgs), the flux in the peaks of the SED increases by less than 7%. At effective temperatures higher than those shown in Figure 3, a greater change in the spectrum would be expected *in cloudless models*. However, in brown dwarf atmospheres with $T_{\rm eff} \gtrsim$ 1400 K, the continuum opacity of the condensates overwhelms the H_2 CIA opacity and the spectrum is unaffected.

3. AMMONIA OPACITY

In brown dwarf atmospheres, the chemistry of nitrogen is dominated by molecular nitrogen N_2 and ammonia NH_3, the

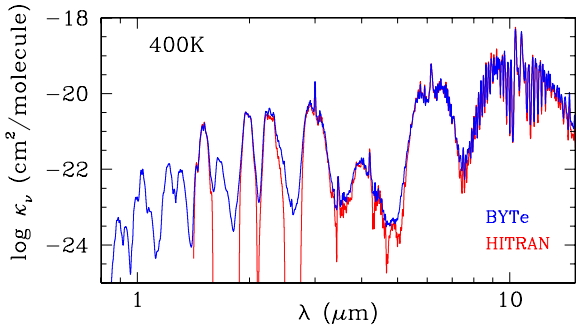

Figure 4. Absorption coefficient of NH_3 at $T = 400$ K and $P = 1$ bar. The red line shows the opacity calculated from the line list that we used in our previous atmosphere models. It is primarily based on the HITRAN data base supplemented with more recent laboratory measurements (Freedman et al. 2008). The blue line labeled "BYTe" shows the absorption coefficient computed from the new first-principles line list of Yurchenko et al. (2011). For clarity, the absorption coefficient is shown at a resolving power of $R = 200$.

(A color version of this figure is available in the online journal.)

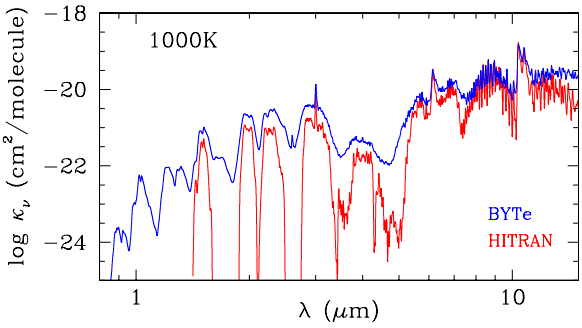

Figure 5. Same as Figure 4 for $T = 1000$ K.

(A color version of this figure is available in the online journal.)

latter being favored at higher pressures and lower temperatures (Lodders & Fegley 2002). The transformation of N_2 into NH_3 occurs at $T_{\rm eff} \sim 800$ K and is, along with the similar conversion of CO to CH_4, one of the most significant chemical changes in brown dwarf atmospheres as $T_{\rm eff}$ decreases. While N_2 has no permanent dipole moment and is effectively invisible in brown dwarf spectra[7], the fundamental band of NH_3 in the 10–11 μm region is seen in T2 and later dwarfs (Cushing et al. 2006) and the entire 9–14 μm region is affected by NH_3 absorption (Saumon et al. 2006). Ammonia has a series of weaker overtone bands in the near-infrared, two of which are centered at 2.0 and 1.5 μm and fall in the K and H photometric bands where the SEDs of T dwarfs show emission. The apparition of these bands in the spectra of very cool brown dwarfs has been suggested as a trigger for a new spectral class (Burrows et al. 2003; Leggett et al. 2007; Kirkpatrick 2008).

Saumon et al. (2000) reported the detection of three NH_3 features in a $R = 3100$ spectrum of the T7p Gliese 229B in the 2.02–2.045 μm range but other expected NH_3 features were missing. This tentative detection was followed by a decade where no other near-infrared spectrum of T dwarfs was taken at high enough resolution in the K band to reveal NH_3 features. The first unambiguous detection of NH_3 in brown dwarfs was achieved with the Infrared Spectrograph (IRS) of the *Spitzer space telescope*, which clearly showed the 10–11 μm band in the combined spectrum of ϵ Indi Bab (T1+T6) (Roellig et al. 2004; Mainzer et al. 2007) and then in all dwarfs of type T2: this was later observed with the IRS (Cushing et al. 2006, 2008; Saumon et al. 2007; Stephens et al. 2009; Leggett et al. 2010b). Recently, the search for extremely cool dwarfs has uncovered several objects with $T_{\rm eff} \lesssim 600$ K where the blue wing of the H-band flux peak appears depressed due the presence of NH_3 (Delorme et al. 2008; Lucas et al. 2010; Liu et al. 2011; Cushing et al. 2011). Finally, a new $R \sim 6000$ near-infrared spectrum of the $T_{\rm eff} \sim 500$ K T9 dwarf UGPS J072227.51−054031.2 contains NH_3 features (Bochanski et al. 2011). The detection of NH_3 in the near-infrared spectrum of several ultracool dwarfs is one of the factors that motivate the creation of the new Y spectral class (Cushing et al. 2011).

The analysis of the spectral signature of NH_3 in T dwarfs is complicated by the presence of vertical mixing in the atmosphere and by the invisibility of N_2. Because the timescale for the conversion of N_2 to NH_3 is very long at low temperatures, gas eddies from very deep in the atmospheres where N_2 and NH_3 are in chemical equilibrium at high temperatures can be transported vertically by convection and slow mixing in the radiative zone to regions of lower temperatures on a timescale which is much shorter than the $N_2 \rightarrow NH_3$ conversion, resulting in a reduced NH_3 abundance (Fegley & Lodders 1994, 1996; Lodders & Fegley 2002; Saumon et al. 2006; Hubeny & Burrows 2007). This process can reduce the observed abundance of NH_3 by factors of 5–10, weakening the NH_3 bands noticeably. Reduced NH_3 absorption in the 9–14 μm region has been found in every T dwarf observed with the *Spitzer* IRS with a high enough signal-to-noise ratio (Saumon et al. 2006, 2007; Mainzer et al. 2007; Burgasser et al. 2008; Leggett et al. 2009, 2010b) and can be fully explained by considering the convective mixing timescale and the timescale for $N_2 \rightarrow NH_3$ conversion. Considering the relatively well-understood chemistry of nitrogen and the universality of a deep convection zone in the atmospheres of brown dwarfs, it is reasonable to assume that the abundance of NH_3 is reduced by vertical transport in all T dwarfs.

In view of the currently very limited opportunities for spectroscopic observations of brown dwarfs in the mid-infrared and the relative ease of near-infrared spectroscopy, the classification of the growing number of very late T dwarfs and of the new Y dwarfs relies primarily on their near-infrared spectral characteristics, where NH_3 figures prominently as a new spectral index indicator (Delorme et al. 2008; Lucas et al. 2010; Cushing et al. 2011; Burgasser et al. 2012) as anticipated by Burrows et al. (2003), Leggett et al. (2007), and Kirkpatrick (2008). The importance of NH_3 as a strong absorber in the mid-infrared, an indicator of non-equilibrium chemistry, and an important marker for the spectral classification of very late T dwarfs and Y dwarfs demands a high-quality line list to compute reliable models.

3.1. New Theoretical NH_3 Line List

Our previous models used an NH_3 line list from the HITRAN data base (Rothman et al. 2003, 2005, 2009) supplemented with room temperature data in the 0.6–0.7 μm^{-1} range (Freedman et al. 2008; Sharp & Burrows 2007). In principle, the fundamental band at 10–11 μm should be well represented in the low temperature ($\sim$300 K) HITRAN data base, but the line list becomes increasingly incomplete at shorter wavelengths and higher temperatures. The resulting opacity at 400 and 1000 K is shown in Figures 4 and 5. There are several gaps in the interband regions 2.5–2.75 μm, $\sim$2.11 μm, and 1.6–1.88 μm, and the list stops at 1.42 μm. Such a line list is inadequate to analyze the rapidly growing spectroscopic data for $T_{\rm eff} \lesssim 600$ K

[7] Like H_2, N_2 causes CIA (Borysow & Frommhold 1986b, 1987), but its mole fraction of $\sim 10^{-4.2}$ makes this contribution to the opacity in brown dwarf atmospheres completely negligible.

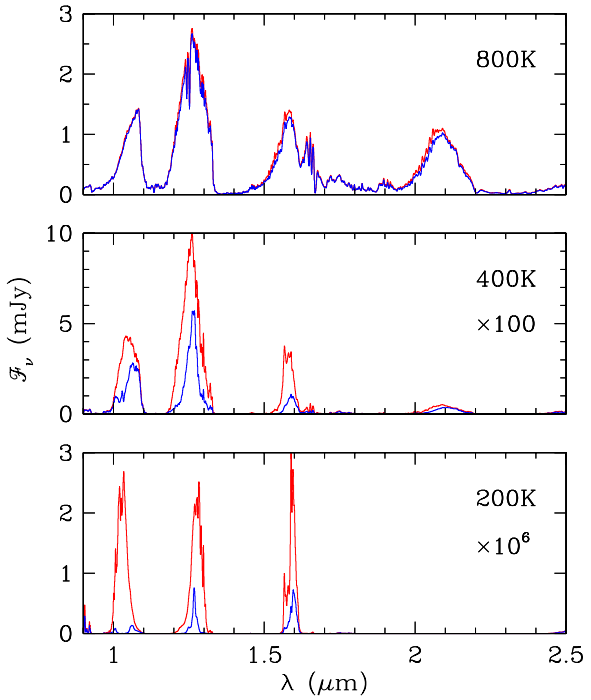

Figure 6. Effect of the new NH_3 opacity on near-infrared spectra of cool brown dwarfs. Three models are shown with $T_{\rm eff}$ = 800, 400, and 200 K. All models shown have solar composition, $\log g = 4$, are cloudless and in chemical equilibrium. Models computed with the HITRAN line list for NH_3 are shown in red while those computed from the same (T, P) structure but with the BYTe NH_3 line list are in blue. The spectra are shown as absolute fluxes for a distance of 10 pc and at $R = 500$ for clarity.

(A color version of this figure is available in the online journal.)

dwarfs, which has motivated recent experimental (Hargreaves et al. 2011) and theoretical work on ammonia (Huang et al. 2011a, 2011b; Yurchenko et al. 2011).

A new extensive line list for NH_3 has recently been calculated from first principles. It is based on a new potential energy surface (Yurchenko et al. 2005) that has been refined by fitting calculated energy levels to nearly 400 levels that are accurately known experimentally (Yurchenko et al. 2011). The resulting energy levels agree with the experimental values to within 1 cm^{-1} and generally under 0.1 cm^{-1}. This "BYTe" NH_3 line list (Yurchenko et al. 2011) contains over 1.1 billion lines, compared to ∼34,000 in HITRAN. It extends from 0 to 12,000 cm^{-1} (0.83 μm) and is applicable up to 1500 K. An independent calculation of an NH_3 line list is under way (Huang et al. 2011b). Figures 4 and 5 show the improvement of the BYTe line list over the HITRAN opacity. At 400 K, we expect the HITRAN opacity to be quite good since it is based on data acquired primarily at room temperature. This is indeed what the BYTe line list shows as both are nearly identical near the center of all the bands in common between the two line lists. In addition, the BYTe line list includes new bands at 1.65 μm and shortward of 1.4 μm, and contains many weak lines that fill in the inter-band regions where there are gaps in the HITRAN line list. The differences become more dramatic at higher temperatures (Figure 5) where the transitions from thermally excited levels come into play, reducing the contrast between the peaks and valleys of the opacity and increasing the band opacity by factors of ∼3–5 compared to the HITRAN value. The opacity in the 8–15 μm also increases significantly.

The effect of the change in NH_3 opacity on the synthetic spectra is shown in Figure 6. For this comparison, spectra computed with the HITRAN and the BYTe line lists use the same (T, P) atmosphere structure. At $T_{\rm eff}$ = 1200 K (not shown), the spectra are identical but at $T_{\rm eff}$ = 800 K there is a small flux decrease of $\lesssim$20% on the blue side of both the H and K peaks. At lower $T_{\rm eff}$, the chemical equilibrium shifts to strongly favor NH_3 over N_2 as the dominant nitrogen bearing species and its opacity become more significant compared to the competing absorption from H_2O and CH_4. This leads to dramatic changes in the spectrum. All the near-infrared flux peaks are reduced by factors of two to four. In particular, the new bands at short wavelengths dramatically affect the shape of the Y and J peaks at $T_{\rm eff}$ = 400 K. At the extremely low $T_{\rm eff}$ of 200 K, the changes are limited to the spectral regions were there are gaps in the HITRAN line list, and lead to very distinctive features in the Y and J bands. In particular, the Y-band peak is split in two. Figure 6 suggests that, in addition to the NH_3–H spectral index which more or less measures the slope of the blue side of the H-band flux peak (Delorme et al. 2008), another NH_3-sensitive index could be defined to measure the curvature of the J-band peak. In the mid-infrared (not shown), the most variation is shown by the 800 K spectrum with a <40% decrease in flux in the 9–15 μm region. The 400 and 200 K spectra are barely affected in the mid-infrared. All these differences decrease somewhat as gravity increases. The spectra shown in Figure 6 and discussed above are computed in chemical equilibrium. However, we expect that the NH_3 abundance will be prevented from coming into equilibrium by convection, resulting in surface abundances ∼10 times lower in the upper atmosphere. Consequently, NH_3 absorption is more muted in non-equilibrium spectra and the changes discussed above are smaller than in models that are in chemical equilibrium. The one exception is the $T_{\rm eff}$ = 200 K model, which is so cold that the entire atmosphere is dominated by NH_3 whose abundance becomes nearly insensitive to convective mixing.

The recently identified Y dwarfs have $T_{\rm eff} \sim$ 300–500 K (Cushing et al. 2011). The spectra computed with the new BYTe line list indicate that broad NH_3 features should be detectable in the near-infrared, most notably as a shoulder on the blue side of the Y-band peak at $T_{\rm eff} \sim$ 400 K which is split at $T_{\rm eff} \lesssim$ 300 K by a growing NH_3 band centered at 1.03 μm. The J-band peak becomes triangular and the H-band peak narrows. The strength of these effects is reduced by the non-equilibrium abundance of NH_3.

4. MODELS INCLUDING BOTH THE NEW H_2 CIA AND NH_3 OPACITIES

We have computed new model atmospheres and synthetic spectra using the new H_2 CIA and NH_3 opacities. In all other aspects, these models are identical to those described in Saumon & Marley (2008) and Marley et al. (2002), with additional details provided in Cushing et al. (2008) and Stephens et al. (2009). These new models, which include cloudless and cloudy atmospheres, were used in the recent analyses presented in Cushing et al. (2011), Luhman et al. (2012), and Leggett et al. (2012). These new cloudless model spectra are compared to our previous models in Figure 7, where, in contrast with Figures 3 and 6, the (T, P) structures are computed with their respective opacities and thus the model structures and spectra are self-consistent. In this case, the flux is redistributed along the SED to conserve the total flux (which was not the case in Figures 3 and 6). At $T_{\rm eff}$ = 1500 and 1000 K, the changes are modest and dominated by the new H_2 CIA opacity. The reduced opacity in the first overtone band of H_2–H_2 CIA is responsible for the

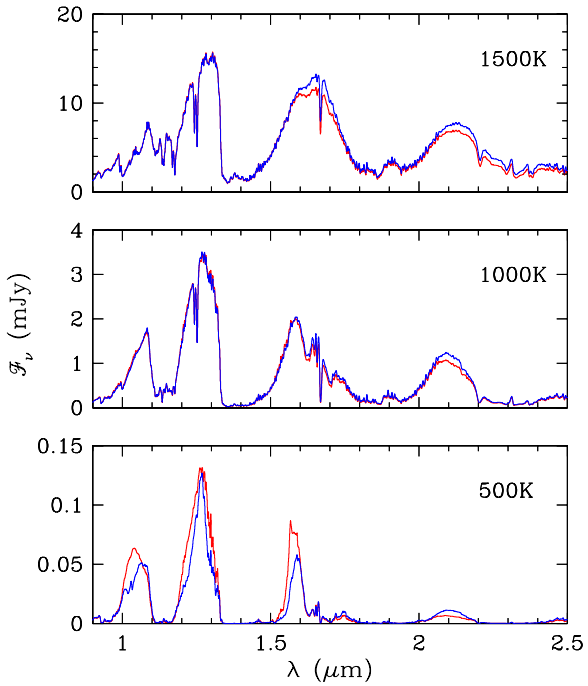

Figure 7. Comparison of spectra including the new H_2 CIA and the BYTe NH_3 opacities (blue) with spectra from a previous generation that only differ in these two sources of opacity (red). These cloudless spectra have $\log g = 5$ (cgs), solar metallicity, and are computed in chemical equilibrium. The effective temperatures are 1500, 1000, and 500 K. In contrast with Figures 3 and 6, the atmospheric (T, P) structures have been computed with the appropriate (old or new) opacities. The spectra are plotted at $R = 500$ for clarity.

(A color version of this figure is available in the online journal.)

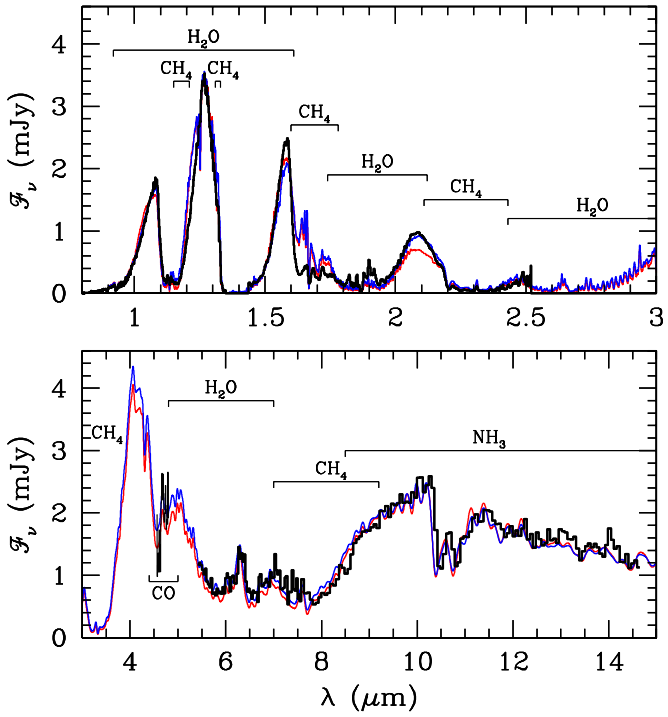

Figure 8. Spectrum of Gliese 570D. The data are shown in black (Burgasser et al. 2003b; Geballe et al. 2001; Cushing et al. 2006; Geballe et al. 2009). The spectrum obtained with our previous models is shown in red (Saumon et al. 2006). The blue curve shows the spectrum computed with the new H_2 CIA and the BYTe NH_3 line list with the same model parameters: $T_{\rm eff} = 820$ K, $\log g = 5.23$ (cgs), [M/H] = 0, and eddy diffusion coefficient $\log K_{zz}$ (cm^2 s^{-1}) = 4.5. The models are plotted at a resolving power of $R = 500$ (top panel) and $R = 100$ (bottom panel), approximating that of the data. The models are not normalized to the data but are fluxes at Earth computed with the known distance of Gl 570D and the radius obtained from the evolution with the above parameters.

(A color version of this figure is available in the online journal.)

increased flux in the K-band peak (∼15%) and a smaller increase in the H-band flux. The $T_{\rm eff} = 1500$ K spectrum also shows a 7% flux increase in the 4 μm peak but the 3–15 μm cloudless spectra are otherwise unaffected. Near the T/Y dwarf transition, where $T_{\rm eff} \sim 500$ K, all four near-infrared peaks in the spectrum are noticeably affected. Absorption by NH_3 changes the shape of the Y and J peaks and shaves off the blue side of the H-band peak. Back warming from this NH_3 absorption pushes the flux out in the K band, which is now ∼75% brighter, and in the 4–8 μm region where the flux increases by ∼30%.

4.1. Comparison with the Spectrum of Gliese 570D

The T7.5 dwarf Gliese 570D (Burgasser et al. 2000) is the most thoroughly studied late T dwarf. Optical, near-infrared, M band, and *Spitzer* IRS spectroscopy are available—sampling ∼70% of the total flux emitted—as well as *Spitzer* IRAC and *WISE* photometry. As this brown dwarf is a companion to a nearby main-sequence star, its distance and metallicity are accurately known and its age is fairly well constrained to 2–5 Gyr. Because Gl 570D is nearby and relatively bright, the whole data set is of high quality and very effectively constrains the models. It is an excellent test object to validate the new models and evaluate the improvements brought about by the new opacities. Detailed analyses of Gl 570D (Geballe et al. 2001, 2009; Saumon et al. 2006) have established that $T_{\rm eff} = 800$–820 K and $\log g = 5.09$–5.23 (cgs), where the ranges of $T_{\rm eff}$ and $\log g$ are correlated: a higher $T_{\rm eff}$ corresponds to a higher gravity. Solar metallicity was adopted based on the metallicity of the primary ([Fe/H] = 0.09 ± 0.04). Saumon et al. (2006) established that convective transport drives the NH_3 abundance below the value expected from chemical equilibrium and obtained a very good fit of the entire SED of Gl 570D (see also Geballe et al. 2009). Figure 8 shows the spectrum computed by Saumon et al. (2006) for those parameters within the above range that best reproduce the data and a new model computed with the same atmospheric parameters but with the new H_2 CIA and NH_3 opacities. There is significant improvement in the K-band peak, which is now fitted very well. There is also a modest improvement in the 5.5–7.5 μm region and beyond 9 μm where NH_3 absorption features overlap with H_2O absorption. The new H_2 CIA calculation, which is primarily responsible for the increased flux in the K band represents a significant improvement over the previously available tabulation. Outside of the 9–14 μm region, NH_3 absorption is rather weak at this $T_{\rm eff}$, and the new NH_3 opacity leads to very modest changes. We believe that the remaining discrepancies in our fit of Gl 570D, such as the width of the J-band peak and the depth of the 1.6 μm band of CH_4, are primarily due to the very incomplete methane line list, which is presently in a similar state as the ammonia line list was prior to the first-principles calculation of Yurchenko et al. (2011).

4.2. Comparison with Near-infrared Photometry

While a comparison with the SED of Gl 570D provides a detailed test of the new models, the overall effect of the new opacities can be better appreciated in color–magnitude diagrams where synthetic colors can be compared to a large set of photometric data. Prior to 2003, our models used the solar

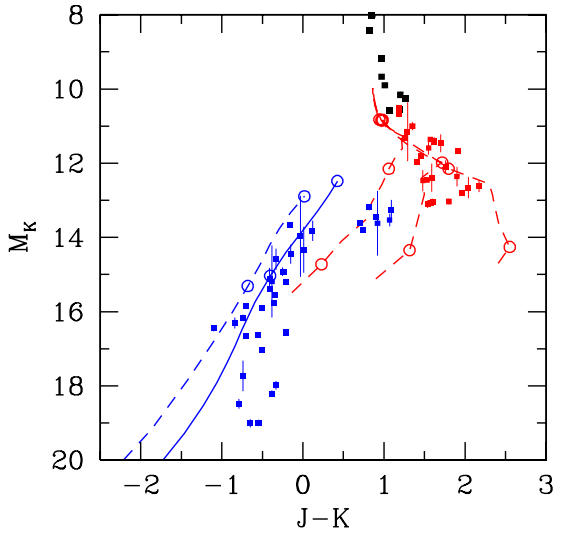

Figure 9. M_K vs. $J-K$ color–color diagram (MKO system) comparing models with the near-infrared photometry of field MLT dwarfs. The photometry is from Leggett et al. (2002), Knapp et al. (2004), and Marocco et al. (2010) with M dwarfs in black, L dwarfs in red, and T dwarfs in blue. All known binaries have been removed from the sample except those with resolved MKO photometry: ϵ Indi B (McCaughrean et al. 2004), SDSS J102109.69−030420.1 and SDSS J042348.57−041403.5 (Burgasser et al. 2006), and Kelu-1 (Liu & Leggett 2005). The parallaxes are from Perryman et al. (1997), Dahn et al. (2002), Tinney et al. (2003), Vrba et al. (2004), Marocco et al. (2010), and various references in Leggett et al. (2002). Solid blue curve: cloudless models calculated with the new H_2 CIA and the BYTe NH_3 line list and an eddy diffusion coefficient $K_{zz} = 10^4$ cm^2 s^{-1} (e.g., these model are not in chemical equilibrium). The curve extends from $T_{\rm eff} = 1500$ K to 500 K, with open circles indicating $T_{\rm eff} = 1500$ K and 1000 K. The dashed blue curve shows models computed with older H_2 CIA and NH_3 opacities and $K_{zz} = 0$ (chemical equilibrium) (Saumon & Marley 2008). The dashed red curves are cloudy models in chemical equilibrium from Saumon & Marley (2008) extending from 2400 K to 900 K with open circles indicating (from the top) $T_{\rm eff} = 2000$, 1500, and 1000 K. Each curve corresponds to a different value of the cloud sedimentation parameter (see Ackerman & Marley 2001; Saumon & Marley 2008) of $f_{\rm sed} = 1$, 2, and 3, from right to left, respectively. Cloudy models computed with the new opacities overlap the cloudy sequences shown. All models shown have solar metallicity and $\log g = 5$.

(A color version of this figure is available in the online journal.)

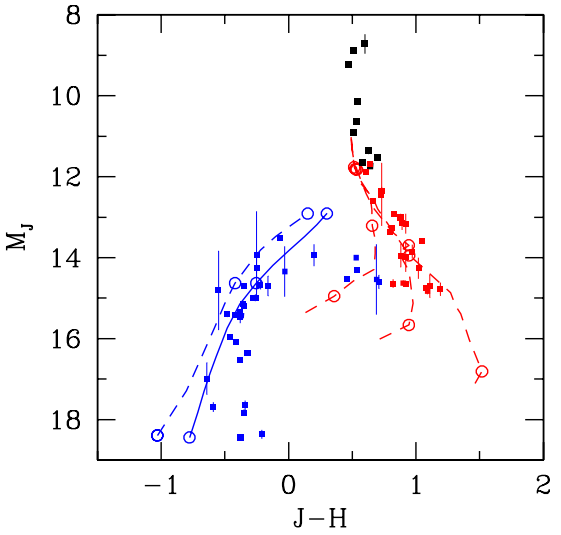

Figure 10. Same as Figure 9 for M_J vs. J–H. The Y0 dwarf WISEP J1541−2250, with $M_J = 23.9 \pm 0.8$ and $J-H = 0.17 \pm 0.63$ (Cushing et al. 2011; Kirkpatrick et al. 2011), falls well outside this figure.

(A color version of this figure is available in the online journal.)

abundances of Lodders & Fegley (1998) and the cloudless sequence was in generally good agreement with the near-infrared colors of late T dwarfs (Burgasser et al. 2002). A significant downward revision of the CNO abundances in the solar photosphere (Allende Prieto et al. 2002) motivated a change of the solar abundances in our models (Lodders 2003) which moved the cloudless sequence to the blue in $J-K$. The resulting sequence of [M/H] = 0 cloudless models are too blue compared to late-field T dwarfs, particularly in $J-K$ when compared to the near-infrared colors of late T field dwarfs (Figures 9 and 10(e) of Saumon & Marley 2008).[8] The new H_2–H_2 CIA has a weaker first overtone band which increases the K-band flux and moves the cloudless models to redder $J-K$, largely compensating for the effect of the reduced CNO abundances (Figure 9). The new sequence of models is still slightly bluer by $\lesssim$0.15 than the late T dwarf sequence, which may be due to missing CH_4 opacity on the J-band peak. The spread of the observed sequence of late T dwarf colors is significant and can be accounted for by the observed distribution in metallicity of field dwarfs (Figure 15(f) of Saumon & Marley 2008). The very latest T dwarfs recently discovered with $M_K \gtrsim 17$ reveal a saturation in $J-K$ and are redder than the calculated cloudless sequences. This may be caused by several limitations in our models, such as the near-infrared opacity of CH_4, the presence of clouds of compounds with low condensation temperature such as Na_2S, or the appearance of water clouds. Note that water condensation is included in the chemistry of the atmosphere and the gas phase H_2O abundance is reduced in the low-$T_{\rm eff}$ models where water condenses. We are investigating the role of clouds in low-$T_{\rm eff}$ atmospheres and the results will be reported in a separate publication. On the other hand, our cloudy sequences account for iron and silicate clouds and reproduce the SEDs and infrared colors of field L dwarfs fairly well (Saumon & Marley 2008; Cushing et al. 2008; Stephens et al. 2009). Cloudy models with $T_{\rm eff} \gtrsim 900$ K are representative of field L dwarfs and the HR 8799 planets (Marley et al. 2012) and are shown in Figure 9. These hotter, cloudy models are barely affected by the new opacities and their near-infrared colors are very nearly identical to the older ones down to $T_{\rm eff} = 900$ K. This is a consequence of the opacity of condensates, which reduces the importance of the H_2 CIA and of the higher temperatures of the cloudy models which reduce the abundance of NH_3.

The same general picture emerges from the M_J versus J–H color–magnitude diagram (Figure 10), although the new cloudless model now represents the J–H sequence of the late-field T dwarfs quite well.[9] The data suggest that the J–H color saturates around −0.6 (see also Kirkpatrick et al. (2011) at $M_J \sim 17$, which is further supported by the position of the Y0 dwarf WISEP J1541−2250 in this color–magnitude diagram ($M_J = 23.9 \pm 0.8$, $J-H = 0.17 \pm 0.63$; Cushing et al. 2011; Kirkpatrick et al. 2011). Our cloudless sequences do show such a minimum in J–H at $T_{\rm eff} \sim 400$ K and a rapid turnover to the red at lower $T_{\rm eff}$. However, the models do not turn over to the red soon enough and reach values of $J-H \sim -1$, which are bluer than is observed. It will be interesting to see how the near-infrared color–magnitude diagrams will be affected by a more complete CH_4 line list when it becomes available or by the inclusion of a water cloud in the models.

[8] Note that the cloudless COND models of Allard et al. (2001) use the older solar abundances of Grevesse & Noels (1993) and agree very well with the observed near-infrared colors of late T dwarfs.

[9] This may be somewhat fortuitous in view of the model limitations mentioned above, particularly the poorly modeled 1.6 μm band of CH_4 which affects the H band (Figure 8)

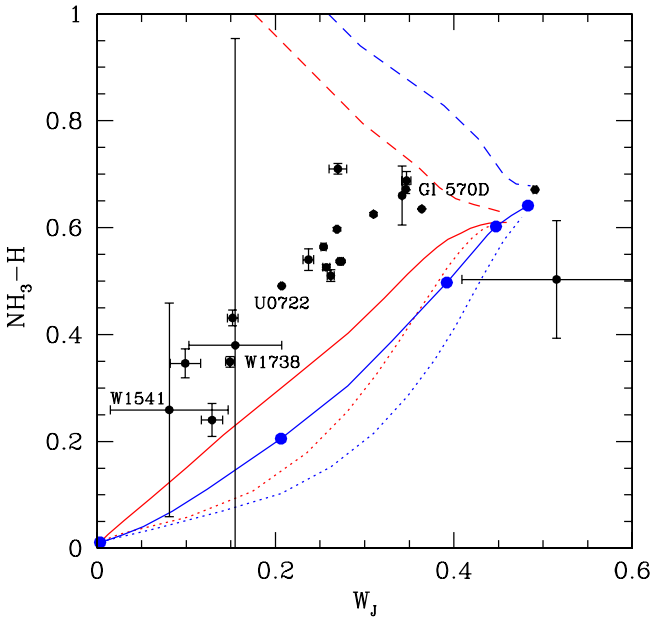

Figure 11. Spectral indices showing the growth of absorption in the blue wing of the H band of late T dwarfs. The spectral indices NH$_3$–H and W_J are defined in Delorme et al. (2008) and Warren et al. (2007), respectively. The curves show the indices computed from cloudless synthetic spectra starting at $T_{\rm eff}$ = 200 (lower left corner) to 1000 K (right) with solid dots marking steps of 200 K. Two gravities, $\log g$ = 4 (cgs, red curves) and 5 (blue), are shown. Dotted lines show models in chemical equilibrium, and solid curves are models driven out of equilibrium by convective transport and mixing in the radiative zone parameterized by the eddy diffusion coefficient $K_{zz} = 10^4$ cm^2 s^{-1}. The dashed lines show spectra computed with the same (T, P) structures after removing the NH$_3$ opacity. The dwarfs Gl 570D (T8, Delorme et al. 2008), UGPS 0722−05 (T9, Cushing et al. 2011), WISEP J1738+2732 (Y0, Cushing et al. 2011), and WISEP J1541−2250 (Y0, Cushing et al. 2011) are labeled. Data were compiled from Warren et al. (2007), Delorme et al. (2008), Burningham et al. (2008), Burningham et al. (2009), Burningham et al. (2011b), Burningham et al. (2011a), Cushing et al. (2011), and Liu et al. (2011).

(A color version of this figure is available in the online journal.)

5. AMMONIA AND Y DWARFS

Increased absorption in the near-infrared has been observed on the blue side of the H-band peak in very late T dwarfs and in the new Y dwarfs, and it is thought to be due to NH$_3$. The strength of the 1.5 μm band of ammonia can be quantified with the NH$_3$–H index defined by Delorme et al. (2008)

$$\mathrm{NH_3}\text{–}H = \frac{\int_{1.53}^{1.56} f(\lambda)\, d\lambda}{\int_{1.57}^{1.60} f(\lambda)\, d\lambda}. \quad (2)$$

Smaller values of NH$_3$–H indicate a relatively low flux on the blue side of the H-band peak that is expected from stronger NH$_3$ absorption. A compilation of the data for the latest dwarfs known is shown in Figure 11. The NH$_3$–H index strongly correlates with the width of the J-band peak (measured by the W_J index; Warren et al. 2007), and with spectral type (Burningham et al. 2008; Cushing et al. 2011), with later types having smaller NH$_3$–H. Figure 11 shows a break in the slope at $W_J \sim 0.3$ corresponding to spectral type T8 (Cushing et al. 2011). Based on the appearance of the blue side of the H-band peak of the Y0 dwarf WISEP J1738+2732—one of the most extreme objects in Figure 11—compared to earlier T8 and T9 dwarfs, Cushing et al. (2011) tentatively ascribe the absorption to NH$_3$.

The models shown in Figure 11 reproduce the observed trend very well and indicate that the reduced abundance of NH$_3$ caused by non-equilibrium chemistry is favored. The dashed lines show the indices computed from the same models after the opacity of NH$_3$ has been removed with a trend that is strongly at odds with the data. The decrease in the modeled NH$_3$–H at $T_{\rm eff} \lesssim 600$ K (or spectral type later than T8) is caused by the 1.5 μm band of NH$_3$. The expectation that NH$_3$ bands would appear in the near-infrared at low enough $T_{\rm eff}$, and its detection as a depression in the blue side of the H-band peak, is thus well supported on a quantitative basis by the models. However, the non-equilibrium models still show a systematic offset from the data, even for the low gravity of $\log g$ = 4 (cgs) which, for these low $T_{\rm eff}$, would correspond to a rather low mass of $\sim$10 M$_{\rm Jupiter}$. It is very likely that the incomplete CH$_4$ line list is responsible for this systematic shift since methane is a strong absorber in the H band and a moderate absorber in the J band (Figure 8).

Without the benefit of models, or with models of limited fidelity, the interpretation of the observed trends in spectral indices can be ambiguous, particularly when considering their variations over a wide range of $T_{\rm eff}$. On the other hand, the direct detection of spectral features provides much more secure evidence of the presence of specific molecular species. While the detection of NH$_3$ in the 2.02–2.045 μm region of the spectrum of the T7p Gl 229B (Saumon et al. 2000) was tentative, Bochanski et al. (2011) identified 11 ammonia features in their medium-resolution ($R \sim 6000$) near-infrared spectrum of the T9 dwarf UGPS 072227.51−054031.2 (here after UGPS 0722−05). Figure 12 shows the portion of their spectrum with the most NH$_3$ features. For comparison, the top curve shows the log of the NH$_3$ opacity computed from the BYTe line list at the conditions corresponding to the atmospheric level where this part of the spectrum is emitted. The lowest curve is an unscaled model spectrum with $T_{\rm eff}$ = 500 K and $\log g$ = 4.25, solar metallicity, and $K_{zz} = 10^4$ cm^2 s^{-1} (Leggett et al. 2012). The six NH$_3$ absorption features identified by Bochanski et al. (2011) in this part of the spectrum all have corresponding troughs in the model spectrum. Four of these features also match peaks in the NH$_3$ opacity, but the other two (1.5264 and 1.5411 μm) do not and their attribution to NH$_3$ is not secure.

To better identify NH$_3$ absorption features in the spectrum of UGPS 0722−05, we show in Figure 12 a spectrum computed from the same atmosphere model but without any NH$_3$ opacity (blue curve). There is obviously much NH$_3$ absorption over the entire range shown, even considering the fact that the model spectrum has a reduced (non-equilibrium) abundance of NH$_3$. This is fully consistent with the smaller value of the NH$_3$–H index of UGPS 0722−05 compared to earlier T dwarfs (Figure 11). However, a careful comparison of the spectra with and without NH$_3$ does not reveal any distinct feature at this spectral resolution. Every feature in one spectrum appears in the other, albeit with a different amplitude. For example, the 1.5142 μm absorption feature matches a peak in the NH$_3$ opacity and an edge in the model spectrum (Figure 12), but that edge also appears in the spectrum computed without NH$_3$, making the attribution doubtful. The model spectrum reproduces individual features of the observed spectrum fairly well (after scaling), but not exactly, which makes the attribution of specific features problematic. We find this to also be the case in other regions where Bochanski et al. (2011) found NH$_3$ features (1.21–1.27 μm, 1.56–1.64 μm, and at 1.990 μm).[10]

[10] For completeness, we note that the two features in the low-resolution ($R \sim 500$) spectrum of UGPS 0722−05 pointed out by Lucas et al. (2010) at $\sim$1.275 μm and at $\sim$1.282 μm can be identified with synthetic spectra at higher resolution as blends of H$_2$O features. A weaker blend of H$_2$S features also contributes to the latter.

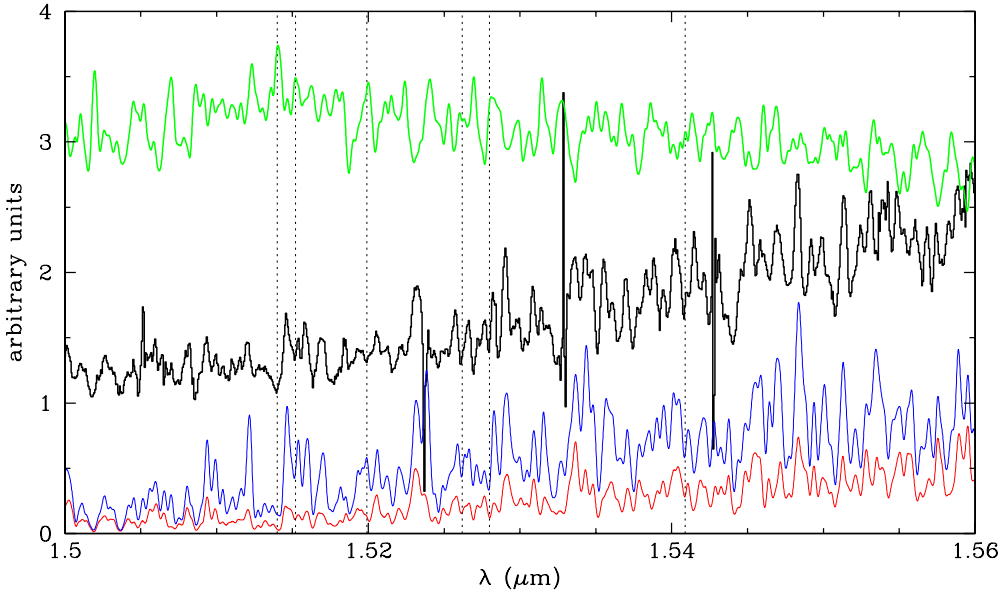

Figure 12. Medium-resolution spectrum ($R \sim 6000$) of UGPS 0722−05 (Bochanski et al. 2011) (black). The observed spectrum has been rescaled, shifted vertically, and the radial velocity (47 km s^{-1}; Bochanski et al. 2011) has been removed. A cloudless synthetic spectrum, with $T_{\rm eff} = 500$ K, $\log g = 4.25$, [M/H] = 0, $K_{zz} = 10^4$ cm^2 s^{-1} (Leggett et al. 2012) is shown in red. The blue curve represents the same spectrum calculated without any NH_3 opacity. The $\log_{10}$ of the NH_3 opacity at 650 K and 1 bar, corresponding to the emission level of this part of the spectrum in the model, is shown in green at an arbitrary scale. The model spectra and the opacity are shown at the spectral resolution of the data. The vertical dotted lines show the NH_3 absorption features identified by Bochanski et al. (2011) in the spectrum of UGPS 0722−05 which should correspond to peaks in the NH_3 opacity.

(A color version of this figure is available in the online journal.)

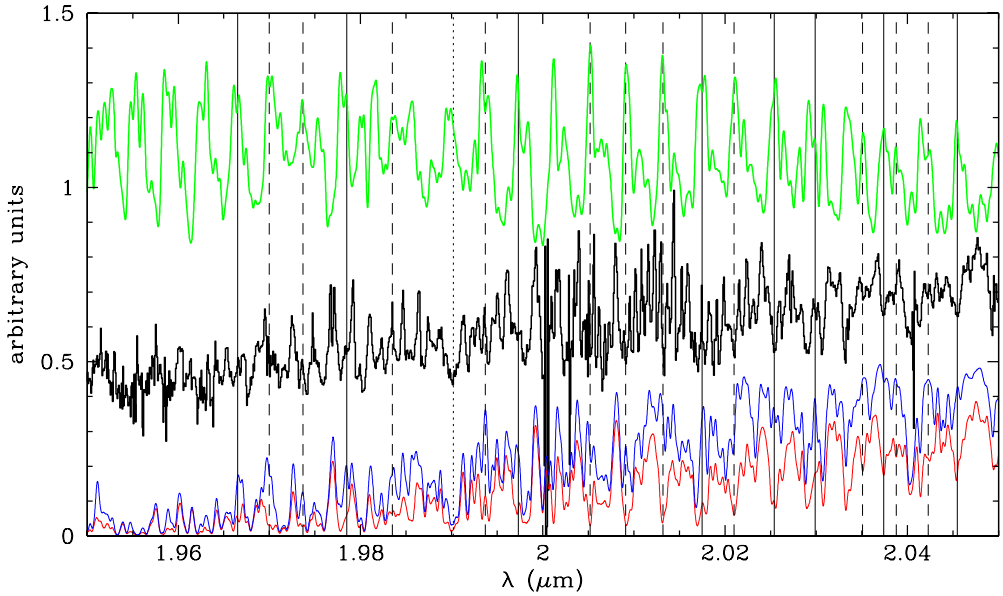

Figure 13. Same as Figure 12 but in the K band. The models have been rescaled for clarity. The vertical dotted line shows the NH_3 feature identified by Bochanski et al. (2011) in the spectrum of UGPS 0722−05. The other vertical lines are NH_3 absorption features predicted by the model spectrum, which all match peaks in the NH_3 opacity. Those that are also apparent in the data are shown with solid lines while those that are ambiguous or missing are shown with dashed lines.

(A color version of this figure is available in the online journal.)

The situation is different in the 1.96–2.05 μm spectral region where Saumon et al. (2000) found three ammonia features in Gl 229B. Figure 13 shows this spectral region with the same models and opacity shown in Figure 12 (with different scalings for clarity). The vertical solid and dashed lines correspond to 19 NH_3 absorption features that are clearly identifiable from the difference between the spectrum computed with the non-equilibrium NH_3 abundance (red) and the spectrum computed without NH_3 opacity (blue). In this spectral range, almost every peak in the NH_3 opacity (green) corresponds to a distinct absorption feature in the synthetic spectrum. The solid lines identify eight absorption features that are present in the spectrum of UGPS 0722−05,[11] and the dashed lines indicate six NH_3 features that are not clearly detected in the spectrum and five that appear to be missing. Two of the detected features (2.0374 and 2.0455 μm) match those found in Gl 229B by Saumon et al. (2000). An absorption feature clearly identified in Bochanski

[11] If we ignore the single high-valued pixel making up the spike in the data at 2.0175 μm, the NH_3 feature stands out.

et al. (2011) at 1.9905 μm (dotted line) corresponds to a well-defined absorption feature in the model spectrum. This feature is barely affected by the removal of all NH_3 opacity, however, and does not match very well with the NH_3 opacity peak centered at 1.9896 μm. In our model spectrum, this absorption is caused by H_2O.

We conclude that the detection of ammonia absorption features in the near-infrared spectra of very late T dwarfs and Y dwarfs is easier in the *K* band near 2 μm than in the *H* band near 1.53 μm. The main reason for this is that the NH_3 opacity in the *K* band is composed of a series of more or less equally spaced and well-separated peaks (Figure 13), while in the *H* band it has a denser irregular structure with a smaller dynamic range as well as a peak opacity that is about one order of magnitude smaller (Figures 12 and 4). With higher resolving power it becomes possible to isolate NH_3 features in the *H* band. For example, with $R \sim 20{,}000$, about a dozen features stand out in the 1.51–1.57 μm region of the model shown in Figure 12. For dwarfs cooler than ~400 K, the condensation of water becomes significant (Burrows et al. 2003), removing H_2O from the gas and unmasking the NH_3 bands. For instance, the blue side of the *H*-band peak becomes completely dominated by NH_3 absorption, and NH_3 features should be readily detectable in the spectrum. This is also true in the 2–2.05 μm region, although the flux is much lower than at 1.55 μm. The NH_3 bands will thus become stronger with lower $T_{\rm eff}$ until ammonia itself begins to condense at $T_{\rm eff} \sim 160$ K (Burrows et al. 2003).

6. CONCLUSION

We have computed new cloudy and cloudless models and synthetic spectra[12] of brown dwarf atmospheres using recent first-principles calculations of the opacity of NH_3 and of the CIA of H_2. Both constitute very significant theoretical improvements in the modeling of the opacity and, in the case of NH_3, the BYTe line list greatly expands over the HITRAN line list which is based primarily on experimental results. The cloudy models, relevant to L dwarfs, are barely affected by the new opacity because of their higher $T_{\rm eff}$ where NH_3 has a very low abundance of the condensate opacity that largely conceals the H_2 CIA.[13] We have thus focused on the role of these two opacities in cloudless models, which are relevant to spectral types ~ T4 and later.

The most notable change in the CIA is a reduction of the opacity in the first roto-vibrational band centered at ~0.42 μm^{-1} (2.4 μm), resulting in an increased *K*-band flux. This corrects a deficiency in our earlier fit of the SED of Gl 570D (Saumon et al. 2006) and we now obtain a remarkable fit of nearly the entire SED of this late T dwarf (Figure 8). Another consequence is that the cloudless sequence shifts toward bluer colors in near-infrared color–magnitude diagrams and is in much better agreement with the colors of the late T dwarfs in the field. This new accurate H_2 CIA opacity will strengthen the analysis of gravity and metallicity indicators in the spectra of late T dwarfs and L subdwarfs and help reduce the uncomfortably large uncertainty in spectroscopic determinations of the gravity of brown dwarfs.

The new BYTe line list for NH_3 greatly improves the near-infrared opacity of ammonia by adding several new bands at short wavelengths as well as a very large number of "hot transitions" that fill in gaps in the HITRAN line list. We can now reliably calculate the opacity of NH_3 at temperatures of several hundreds of degrees, which is crucial even for the coolest known dwarfs as the *Y*, *J*, and *H* bands typically probe temperatures well above $T_{\rm eff}$. The importance of this line list for the study of the T/Y transition and the new Y dwarfs cannot be overstated. Our models show that NH_3 develops very distinct signatures in the *Y*- and *J*-band flux peaks, and confirms the tentative identification of eight other NH_3 absorption features on the blue side of the *H*-band peak which had been anticipated by Burrows et al. (2003). More quantitatively, the new models reproduce the trend in the spectral indices NH_3–*H* and W_J, confirming that the rapid decrease in NH_3–*H* at spectral types later than T8 is due to NH_3 absorption. Thus, all the new *WISE* objects assigned to the Y dwarf class by Cushing et al. (2011) show NH_3 absorption in the *H* band. Furthermore, the data favors models where vertical transport reduces the NH_3 abundance in the observable part of the atmosphere. At a more detailed level, the medium-resolution near-infrared spectrum of the T9 UGPS 0722−05 (Bochanski et al. 2011) provides a rare opportunity to compare data with the detailed predictions of spectral features by the models and of the underlying molecular opacities. While we found that none of the features pointed out by Bochanski et al. (2011) can be unambiguously attributed to NH_3, our new models allow the identification of nine other NH_3 absorption features around 2 μm. The models clearly show that while there is strong NH_3 absorption in the *H* band in late T dwarfs and in the Y0 dwarfs, the general behavior of the NH_3 absorption in the 1.55 μm region makes it more difficult to isolate individual features than in the 2.0 μm region, requiring a resolving power of the order of $R \sim 20{,}000$, compared to ~6000 in the *K* band.

Despite the progress that we have demonstrated here, obvious problems remain with the models. For instance, the fit of Gl 570D still has discrepancies that stand out. The near-infrared color–magnitude diagrams for field dwarfs fail to reproduce the saturation (and possible turnover) revealed by the data at very low $T_{\rm eff}$. The spectral indices NH_3–*H* and W_J do not yet provide a quantitative diagnostic of the atmospheric structure and chemistry. With these two new calculations of molecular opacities that primarily affect late T dwarfs and the new class of Y dwarfs, reliable opacities are available for all important gas phase absorbers except for CH_4. The inadequacy of the current line list of methane has been much maligned ever since the very first spectral modeling of a T dwarf (Marley et al. 1996; Allard et al. 1996). We believe that for cloudless atmosphere models, the CH_4 opacity is the only remaining obstacle of significance to modeling the spectroscopic data accurately. The availability of a CH_4 line list comparable in quality and scope to the BYTe NH_3 line list would open the door to reliable determinations of T dwarf gravities and metallicities, two fundamental parameters that have remained elusive for the vast majority of brown dwarfs.

D.S., M.S.M., and R.S.F. acknowledge support from NASA Astrophysics Theory grant NNH11AQ54I. L.F. and M.A. thank K.L.C. Hunt and her associates for the quantum chemical results provided to us prior to publication, which made their work possible. L.F. and M.A. also acknowledge NSF support through grants AST0708496 and AST0709106.

[12] The synthetic spectra are available upon request to D. Saumon (dsaumon@lanl.gov).

[13] This is no longer the case in low-metallicity L subdwarfs where H_2 CIA is noticeable (Burgasser et al. 2003a, 2009; Cushing et al. 2009).

REFERENCES

Abel, M., Frommhold, L., Li, X., & Hunt, K. L. C. 2011, J. Chem. Phys., 115, 6805

Abel, M., Frommhold, L., Li, X., & Hunt, K. L. C. 2012, J. Chem. Phys., 136, 044319

Ackerman, A. S., & Marley, M. S. 2001, ApJ, 556, 872

Allard, F., Hauschildt, P. H., Alexander, D. R., Tamanai, A., & Schweitzer, A. 2001, ApJ, 556, 357
Allard, F., Hauschildt, P. H., Baraffe, I., & Chabrier, G. 1996, ApJ, 465, L123
Allende Prieto, C., Lambert, D. L., & Asplund, M. 2002, ApJ, 573, L137
Barber, R. J., Tennyson, J., Harris, G. J., & Tolchenov, R. N. 2006, MNRAS, 368, 1087
Bergeron, P., Saumon, D., & Wesemale, F. 1995, ApJ, 443, 764
Bochanski, J. J., Burgasser, A. J., Simcoe, R. A., & West, A. A. 2011, AJ, 142, 169
Borysow, A. 2002, A&A, 390, 779
Borysow, A., & Frommhold, L. 1986a, ApJ, 304, 849
Borysow, A., & Frommhold, L. 1986b, ApJ, 311, 1043
Borysow, A., & Frommhold, L. 1987, ApJ, 320, 437
Borysow, A., Frommhold, L., & Moraldi, M. 1989, ApJ, 336, 495
Borysow, A., Jorgensen, U. G., & Fu, Y. 2001, J. Quant. Spec. Radiat. Transf., 68, 235
Burgasser, A. J. 2004, ApJ, 614, L73
Burgasser, A. J., Gelino, C. R., Cushing, M. C., & Kirkpatrick, D. J. 2012, ApJ, 745, 26
Burgasser, A. J., Kirkpatrick, J. D., Brown, M. E., et al. 2002, ApJ, 564, 421
Burgasser, A. J., Kirkpatrick, J. D., Burrows, A., et al. 2003a, ApJ, 592, 1186
Burgasser, A. J., Kirkpatrick, J. D., Cruz, K. L., et al. 2006, ApJS, 166, 585
Burgasser, A. J., Kirkpatrick, J. D., Cutri, R. M., et al. 2000, ApJ, 531, L57
Burgasser, A. J., Kirkpatrick, J. D., Liebert, J., & Burrows, A. 2003b, ApJ, 594, 510
Burgasser, A. J., Tinney, C. G., Cushing, M. C., et al. 2008, ApJ, 689, L53
Burgasser, A. J., Witte, S., Helling, Ch., Sanderson, R. E., Bochanski, J. J., & Hauschildt, P. H. 2009, ApJ, 697, 148
Burningham, B., Leggett, S. K., Homeier, D., et al. 2011a, MNRAS, 414, 3590
Burningham, B., Lucas, P. W., Leggett, S. K., et al. 2011b, MNRAS, 414, L90
Burningham, B., Pinfield, D. J., Leggett, S. K., et al. 2008, MNRAS, 391, 320
Burningham, B., Pinfield, D. J., Leggett, S. K., et al. 2009, MNRAS, 395, 1237
Burrows, A., Ram, R. S., Bernath, P., Sharp, C. M., & Milsom, J. A. 2002, ApJ, 577, 986
Burrows, A., & Sharp, C. M. 1999, ApJ, 512, 843
Burrows, A., Sudarsky, D., & Lunine, J. I. 2003, ApJ, 596, 587
Cushing, M. C., Kirkpatrick, J. D., Gelino, C. R., et al. 2011, ApJ, 743, 50
Cushing, M. C., Looper, D., Burgasser, A. J., et al. 2009, ApJ, 696, 986
Cushing, M. C., Marley, M. S., Saumon, D., et al. 2008, ApJ, 678, 1372
Cushing, M. C., Roellig, T. L., Marley, M. S., et al. 2006, ApJ, 648, 614
Dahn, C. C., Harris, H. C., Vrba, F. J., et al. 2002, AJ, 124, 1170
Delorme, P., Delfosse, X., Albert, L., et al. 2008, A&A, 482, 961
Dulick, M., Bauschlicher, C. W., Jr., Burrows, A., et al. 2003, ApJ, 594, 651
Fegley, B. J., & Lodders, K. 1994, Icarus, 110, 117
Fegley, B. J., & Lodders, K. 1996, ApJ, 472, L37
Freedman, R. S., Marley, M. S., & Lodders, K. 2008, ApJS, 174, 504
Frommhold, L. 1993, Collision-induced Absorption in Gases (Cambridge: Cambridge Univ. Press)
Frommhold, L., Abel, M., Wang, F., et al. 2010, Mol. Phys., 108, 2265
Geballe, T. R., Saumon, D., Golimowski, D. A., et al. 2009, ApJ, 695, 844
Geballe, T. R., Saumon, D., Leggett, S. K., et al. 2001, ApJ, 556, 373
Goorvitch, D. 1994, ApJS, 95, 535
Grevesse, N., & Noels, A. 1993, in Origin and Evolution of the Elements, ed. N. Prantos, E. Vangioni-Flam, & M. Casse (Cambridge: Cambridge Univ. Press), 14
Gustafsson, M., & Frommhold, L. 2003, A&A, 400, 1161
Hare, W. F. J., & Welsh, H. L. 1958, Can. J. Phys., 36, 88
Hargreaves, R. J., Li, G., & bernath, P. F. 2011, ApJ, 735, 111
Huang, X., Schwenke, D. W., & Lee, T. J. 2011a, J. Chem. Phys., 134, 044320
Huang, X., Schwenke, D. W., & Lee, T. J. 2011b, J. Chem. Phys., 134, 044321
Hubeny, I., & Burrows, A. 2007, ApJ, 669, 1248
Jacquinet-Husson, N., Arie, E., Ballard, J., et al. 1999, J. Quant. Spec. Radiat. Transf., 62, 205
Jacquinet-Husson, N., Scott, N. A., Chdin, A., et al. 2005, J. Quant. Spec. Radiat. Transf., 95, 429
Jorgensen, U. G., Hammer, D., Borysow, A., & Falkesgaard, J. 2000, A&A, 361, 283
Kirkpatrick, J. D. 2005, ARA&A, 43, 195
Kirkpatrick, J. D. 2008, in ASP Conf. Ser. 384, 14th Cambridge Workshop on Cool Stars, Stellar Systems, and the Sun, ed. G. T. van Belle (San Francisco, CA: ASP), 85
Kirkpatrick, J. D., Cushing, M. C., Gelino, C. R., et al. 2011, ApJS, 197, 19
Kirkpatrick, J. D., Reid, I. N., Liebert, J., et al. 1999, ApJ, 519, 802
Knapp, G. R., Leggett, S. K., Fan, X., et al. 2004, AJ, 127, 3553
Leggett, S. K., Burningham, B., Saumon, D., et al. 2010a, ApJ, 710, 1627
Leggett, S. K., Cushing, M. C., Saumon, D., et al. 2009, ApJ, 695, 1517
Leggett, S. K., Golimowski, D. A., Fan, X., et al. 2002, ApJ, 564, 452
Leggett, S. K., Marley, M. S., Freedman, R. S., et al. 2007, ApJ, 667, 537
Leggett, S. K., Saumon, D., Burningham, B., et al. 2010b, ApJ, 720, 252
Leggett, S. K., Saumon, D., Marley, M. S., et al. 2012, ApJ, 748, 74
Liu, M. C., Delorme, P., Dupuy, T. J., et al. 2011, ApJ, 740, 108
Liu, M. C., & Leggett, S. K. 2005, ApJ, 634, L616
Lodders, K. 2002, ApJ, 577, 974
Lodders, K. 2003, ApJ, 591, 1220
Lodders, K., & Fegley, B. 1998, The Planetary Scientist's Companion (Oxford: Oxford Univ. Press)
Lodders, K., & Fegley, B. 2002, Icarus, 155, 393
Lucas, P. W., Tinney, C. G., Burningham, B., et al. 2010, MNRAS, 408, L56
Luhman, K. L., Burgasser, A. J., Labbé, I., et al. 2012, ApJ, 744, L135
Mainzer, A. K., Roellig, T. L., Saumon, D., et al. 2007, ApJ, 662, 1245
Marley, M. S., Saumon, D., Cushing, M. C., & Fortney, J. J. 2012, ApJ, submitted
Marley, M. S., Saumon, D., Guillot, T., et al. 1996, Science, 272, 1919
Marley, M. S., Seager, S., Saumon, D., et al. 2002, ApJ, 568, 335
Marocco, F., Smart, R. L., Jones, H. R. A., et al. 2010, A&A, 524, 38
McCaughrean, M. J., Close, L. M., Scholz, R.-D., et al. 2004, A&A, 413, 1029
Noll, K. S., Geballe, T. R., Leggett, S. K., & Marley, M. S. 2000, ApJ, 541, L75
Partridge, H., & Schwenke, D. W. 1997, J. Quant. Spec. Radiat. Transf., 53, 373
Perryman, M. A. C., Lindegren, L., Kovalevsky, J., et al. 1997, A&A, 323, L49
Plez, B. 1998, A&A, 337, 495
Richard, C., Gordon, I. E., Rothman, L. S., et al. 2012, J. Quant. Spec. Radiat. Transf., in press
Roellig, T. L., Van Cleve, J. E., Solan, G. C., et al. 2004, ApJS, 154, 418
Rothman, L. S., Barbe, A., Benner, C. D., et al. 2003, J. Quant. Spec. Radiat. Transf., 82, 5
Rothman, L. S., Gordon, I. E., Barbe, A., et al. 2009, J. Quant. Spec. Radiat. Transf., 110, 533
Rothman, L. S., Jacquemart, D., Barbe, A., et al. 2005, J. Quant. Spec. Radiat. Transf., 96, 139
Saumon, D., Geballe, T. R., Leggett, S. K., et al. 2000, ApJ, 541, 374
Saumon, D., & Marley, M. S. 2008, ApJ, 689, 1327
Saumon, D., Marley, M. S., Cushing, M. C., et al. 2006, ApJ, 647, 552
Saumon, D., Marley, M. S., Leggett, S. K., et al. 2007, ApJ, 656, 1136
Schwenke, D. 1998, Faraday Discuss., 109, 321
Schwenke, D. 2002, Spectrochim. Acta A, 58, 849
Sharp, C. M., & Burrows, A. 2007, ApJS, 168, 140
Stephens, D. C., Leggett, S. K., Cushing, M. C., et al. 2009, ApJ, 702, 154
Tinney, C. G., Burgasser, A. J., & Kirkpatrick, J. D. 2003, AJ, 126, 975
Vrba, F. J., Henden, A. A., Luginbuhl, C. B., et al. 2004, AJ, 127, 2948
Warren, S. J., Mortlock, D. J., Leggett, S. K., et al. 2007, MNRAS, 381, 1400
Yurchenko, S. N., Barber, R. J., & Tennyson, J. 2011, MNRAS, 413, 1828
Yurchenko, S. N., Barber, R. J., Tennyson, J., Thiel, W., & Jensen, P. 2011, J. Mol. Spec., 268, 123
Yurchenko, S. N., Zheng, J., Lin, H., Jensen, P., & Thiel, W. 2005, J. Chem. Phys., 123, 134308